Measurement Science and Technology

PAPER

Novel method for measuring a dense 3D strain map of robotic flapping wings

IOP Publishing

Measurement Science and Technology

Meas. Sci. Technol. **29** (2018) 045402 (13pp)

https://doi.org/10.1088/1361-6501/aaa4cc

Novel method for measuring a dense 3D strain map of robotic flapping wings

Beiwen Li[1] and Song Zhang[2]

[1] Department of Mechanical Engineering, Iowa State University, Ames, IA 50011, United States of America

[2] School of Mechanical Engineering, Purdue University, West Lafayette, IN 47907, United States of America

E-mail: beiwen@iastate.edu

Received 26 August 2017, revised 7 December 2017
Accepted for publication 3 January 2018
Published 14 March 2018

Abstract

Measuring dense 3D strain maps of the inextensible membranous flapping wings of robots is of vital importance to the field of bio-inspired engineering. Conventional high-speed 3D videography methods typically reconstruct the wing geometries through measuring sparse points with fiducial markers, and thus cannot obtain the full-field mechanics of the wings in detail. In this research, we propose a novel system to measure a dense strain map of inextensible membranous flapping wings by developing a superfast 3D imaging system and a computational framework for strain analysis. Specifically, first we developed a 5000 Hz 3D imaging system based on the digital fringe projection technique using the defocused binary patterns to precisely measure the dynamic 3D geometries of rapidly flapping wings. Then, we developed a geometry-based algorithm to perform point tracking on the precisely measured 3D surface data. Finally, we developed a dense strain computational method using the Kirchhoff–Love shell theory. Experiments demonstrate that our method can effectively perform point tracking and measure a highly dense strain map of the wings without many fiducial markers.

Keywords: flapping wings, superfast 3D imaging, digital fringe projection, geodesics, strain analysis

S Supplementary material for this article is available online

(Some figures may appear in colour only in the online journal)

1. Introduction

Over the past several decades, scientific studies of insect flight have been greatly advanced with new experimental techniques ranging from measurements of flow field to aerodynamics of flight. Within insect flight studies, insect wing deformation and strain have been interesting topics to scientists owing to their variety between different species, between different flight types of the same insect and even between different strokes of the same type of flight [1]. In addition, the deformation and strain of wings could contain important information for lift force analysis [2], which could provide vital insightful knowledge for flapping wing design.

In the past, scientists have made great attempts to study insect wing deformation by first identifying some general patterns of bending during the wing stroke cycles using still photographs [3]. In recent decades, scientists have started to use optical techniques to quantify the deformation of wings. Scientists first attempted to actively illuminate thin laser strips onto the flapping wings, and quantify the wing deformation by analyzing the distorted stripes captured by high-speed cameras [2, 4–7]. However, as shown in figure 1(a), the spatial resolutions of such methods are limited by the sparsely illuminated 'comb-shape'-like laser stripes. Moreover, it is difficult to track any specific points on the wings with such methods [8].

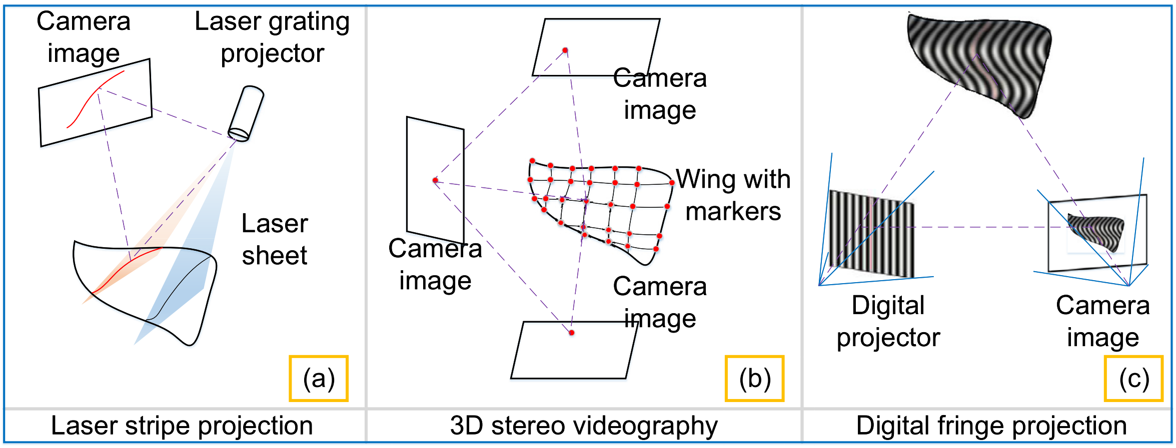

Figure 1. A schematic diagram of (a) the laser stripe projection technology, (b) the 3D stereo videography technology, and (c) the digital fringe projection technology.

To overcome the latter limitation, scientists started to use high-speed stereo videography [9] to provide quantitative descriptions of wing morphology. Within this technique, one of the widely adopted methods is to use fiducial markers as joints to facilitate identification of similar points in different cameras, and 3D information of those joints can be obtained by the well-established stereo vision technique. The geometry of the wings can be reconstructed through the joint-based hierarchical subdivision surface method [8, 9]. A schematic diagram of this method is shown in figure 1(b). Over the years, high-speed videography techniques have been widely adopted to study a variety of species including hummingbirds [10, 11], moths [12], dragonflies [8], butterflies [13], bats [14], etc. An important advantage of such methods is that some specific points (e.g. marker points) can be tracked in different frames to accurately quantify the motion and deformations of those points of interest. However, since this stereo vision based technique hinges on identifying similar points in different camera perspectives, a major limitation of this method is that only those sparsely arranged marker points are precisely measured, albeit the rest of the points can be interpolated through geometric modeling methods [8]. This makes it challenging for performing high-resolution deformation and strain analysis. In reality, for a deformable flying structure, performing high-resolution mechanics testing is of great value for analyzing its fluid-structure interactions [15]. Therefore, it is important to develop technologies that can perform high-resolution mechanics evaluation.

Different from the high-speed stereo videography method, the digital fringe projection (DFP) technique can reconstruct 3D geometries of the entire scene with high resolution and accuracy [16]. As shown in figure 1(c), a DFP technique essentially uses a video projector to illuminate sinusoidal patterns onto the sampled surface, and a camera from another viewing angle is to capture the distorted fringe patterns to obtain 3D information through fringe analysis. Its high spatial resolution makes it possible to realize full-field strain analysis if the dynamic deforming process of the flapping wings can be captured. In this research, we investigate a special type of flapping wing made of an inextensible thin membrane. First, we developed a DFP system to measure the dynamic 3D geometries of the rapidly deforming wings. Specifically, we use a digital-light-processing (DLP) projector to project binary defocused patterns on the wings at 5000 Hz. A precisely synchronized camera captures the distorted fringe patterns by the object surface. The captured distorted patterns are analyzed by a fringe analysis method for 3D topological reconstruction. Once the dynamic 3D geometries are precisely measured, the strain for each point can be computed through examining the geometric deformations. In this research, we also develop a strain analysis framework based on geodesic computation and the Kirchhoff–Love shell theory. We first develop a novel point tracking method based on surface geometry using a proposed method that enhances the Dijkstra's algorithm [17]. The Green–Lagrange strain tensor of each tracked point is then determined by the curvature change from its strain-free condition. Experimental results on 3D reconstruction, validation of point tracking, as well as dynamic evaluation of the strain field demonstrate the success of our proposed method. Our strain analysis framework is solely based on surface geometric information, and thus is advantageous for applications where the measured surface does not contain significant textural variations across the entire image or special surface treatment is undesirable.

Section 2 introduces some theoretical principles and basic technologies related to this research. Section 3 demonstrates the results showing the success of our proposed research. Section 4 discusses the merits and limitations of our work, and section 5 draws a conclusion of this research.

2. Methods

In this section, we will elaborate the theoretical foundations of superfast 3D imaging, our innovated geodesic-based point tracking method, as well as our developed strain computational framework.

2.1. Superfast 3D imaging

We used a modified Fourier transform profilometry (FTP) method [18] for 3D reconstruction. The basic principles can be explained as follows. In theory, two different fringe patterns with a phase shift of π can be described as

$$I_1 = I'(x, y) + I''(x, y)\cos[\phi(x, y)], \tag{1}$$

$$I_2 = I'(x, y) - I''(x, y)\cos[\phi(x, y)], \tag{2}$$

where $I'(x, y)$ stands for the average intensity or DC component, $I''(x, y)$ represents the intensity modulation, and $\phi(x, y)$ is the phase information to be computed. After subtracting the two fringe images, we can get rid of the DC component and obtain

$$I = (I_1 - I_2)/2 = I''(x, y)\cos[\phi(x, y)]. \tag{3}$$

Using Euler's formula, we can reformulate equation (3) as a summation of two harmonic conjugate components:

$$I = \frac{I''(x, y)}{2}\left[\mathrm{e}^{j\phi(x,y)} + \mathrm{e}^{-j\phi(x,y)}\right]. \tag{4}$$

To preserve only one of the two harmonic conjugate components, we can apply a bandpass filter and obtain the final fringe image as

$$I_f(x, y) = \frac{I''(x, y)}{2}\mathrm{e}^{j\phi(x,y)}. \tag{5}$$

In this research, we chose to use a Hanning window as the bandpass filter [18]. After filtering, we can extract the phase through an arctangent function:

$$\phi(x, y) = \tan^{-1}\left\{\frac{\mathrm{Im}\,[I_f(x, y)]}{\mathrm{Re}\,[I_f(x, y)]}\right\}. \tag{6}$$

From equation (6), one can see that the phase ϕ is in the form of an arctangent function. As a result, the extracted phase ϕ is wrapped with a range from $-\pi$ to π. Therefore, phase unwrapping is necessary to obtain an absolute phase map. In this research, we adopted a histogram-based method [19] for absolute phase retrieval.

From equations (1) and (2), we can see that the modified FTP method requires the projection of more than one 8-bit sinusoidal pattern. However, the refresh rate of 8-bit patterns are typically limited to several hundred Hz even for modern DLP projectors (e.g. 247 Hz for Wintech PRO 6500). Consider that our flapping wing robot (e.g. XTIM Bionic Bird Avitron V2.0) flaps 25 cycles per second, this projection speed is not sufficient for high-quality 3D imaging. Alternatively, as introduced by Lei and Zhang [20], one can project 1-bit square binary patterns with projector defocusing to produce a quasi-sinusoidal profile. This method is called the binary defocusing method. The basic principle of the binary defocusing technique is that the projector defocusing effect, which is essentially similar to a Gaussian low-pass filter, can effectively suppress high-order harmonics of a square wave in the Fourier frequency spectrum. Over the past decade, scientists have adopted different methods to further suppress high-order harmonics by means of pulse-width modulation [21], area modulation [22], dithering [23] and so forth. With the reduced data transfer load from 8-bit to 1-bit images, the DLP projectors have enabled kHz 3D shaped measurement speeds [24]. In this research, we used a set of area-modulated patterns [25] for phase extraction and a set of dithered patterns [23] for unwrapping. The fringe pitch for area modulated patterns and dithered patterns are $T = 24$ and $T = 380$ pixels, respectively.

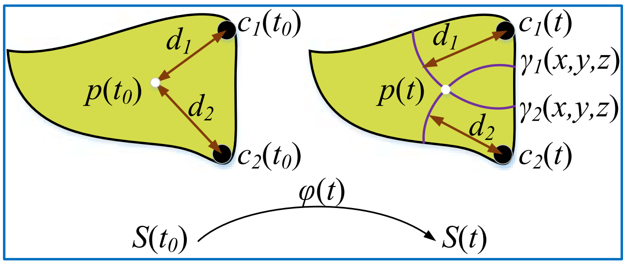

Figure 2. Finding the correspondence between point $p(t_0)$ on the initial surface configuration $S(t_0)$ and point $p(t)$ on the current-deformed configuration $S(t)$; $p(t)$ is identified by finding the intersecting point of the curves $\gamma_1(x, y, z)$ with equal geodesic distance d_1 and $\gamma_2(x, y, z)$ with equal geodesic distance d_2.

2.2. Geodesic-based point tracking

Although we have obtained the 3D data for each frame with superfast 3D imaging, performing strain analysis for each 3D frame is nevertheless challenging since it requires point tracking on the wings so that the strains can be computed by examining the geometric deformations. In this section, we will introduce our proposed geometry-based point tracking method for inextensible membranes assisted by the computation of geodesic distance.

For an inextensible surface, an important property is that the geodesic distances will be retained after surface deformation [26], which provides us with additional constraints to perform point tracking. For any point $p(t_0)$ on the initial surface configuration $S(t_0)$, we need to identify its corresponding point $p(t)$ on a deformed surface configuration $S(t)$. Figure 2 illustrates a schematic diagram of our proposed tracking approach using geodesic computation. Suppose we have two anchor points c_1 and c_2, for any point $p(t_0)$ on an initial undeformed surface $S(t_0)$, we compute its geodesic distances d_1 and d_2, respectively, to the anchor points c_1 and c_2. Then, on the current deformed surface $S(t)$, we extract the curves γ_1 and γ_2, respectively, with equal geodesic distances d_1 and d_2. Finally, we identify the point $p(t)$ by computing the numerical solution of the intersecting point of γ_1 and γ_2. Next, we introduce the detailed procedures of our proposed tracking approach.

The first step of our tracking approach is to compute the geodesic distances of any point $p(t_0)$ to the anchor points c_1 and c_2. The geodesic distance is essentially the length of the shortest distance between two points on the surface. Some well-known computational approaches include Dijkstra's algorithm [17], which is based on distance computation, and the fast marching algorithm [27, 28], which is based on gradient computation. In this research, we developed a computational approach that is based on Dijkstra's algorithm, but optimized to our case by considering that the surface data could contain some noise.

Dijkstra's algorithm finds the shortest path from the a given anchor point on the graph to any other nodes on the graph. Figure 3 shows a simple example of the computational

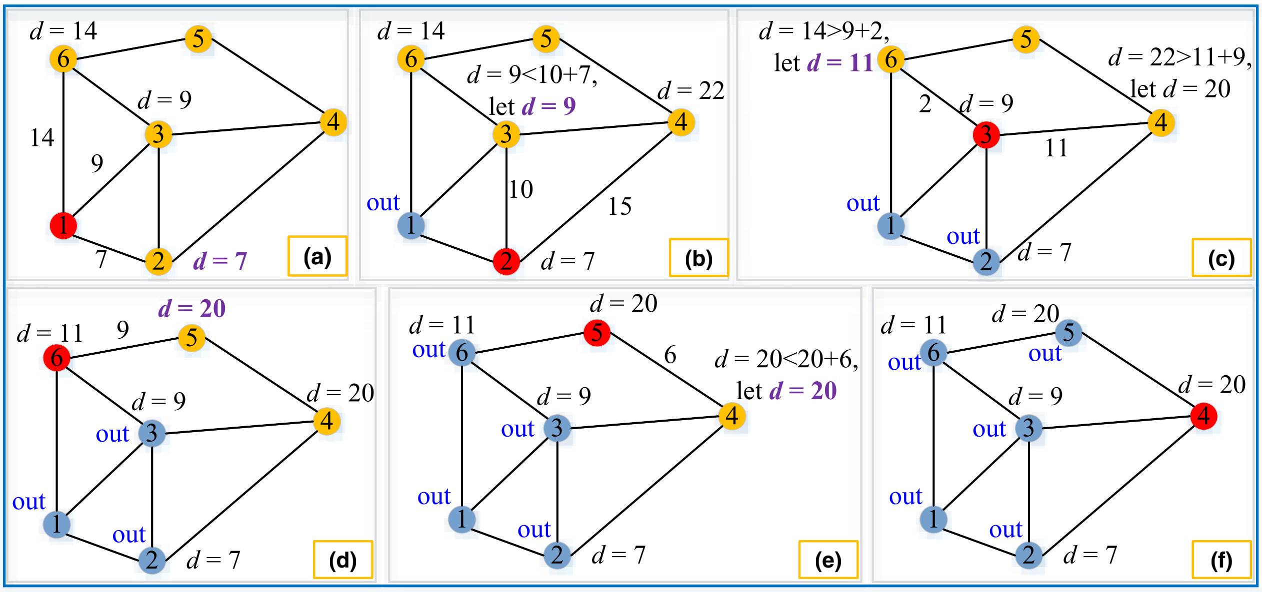

Figure 3. An example of computing the shortest distance by using Dijkstra's algorithm. The numbers between two different nodes denote the length of the path connecting the two nodes. (a)–(f) The computational procedure. Node 1 is the initial anchor point. Each unvisited vertex with the lowest distance becomes the new anchor points, and the old anchor points will not be visited again. Each visited node will have an updated distance value if smaller than the previously marked distance value.

procedure of Dijkstra's algorithm. Suppose node 1 on the graph is the initial anchor point, the distances from which will be computed for each of its neighbors. The one that has the smallest distance becomes the new anchor point, and the previous anchor point will not be visited again and marked as *out*. This procedure continues, and the distance value of each node will be updated whenever a smaller distance value is found. Once all node points have been marked as *out*, the entire procedure is done.

Dijkstra's algorithm performs a good approximation of geodesic computation if the data is ideal and noise-free. However, since our reconstructed 3D data could be 'polluted' by camera noise, here we propose an optimization of the conventional Dijkstra algorithm. The optimization is mainly composed of two parts: (1) selecting a bigger neighborhood window (i.e. 7×7) for possible marching directions; (2) using a fitted cubic Bézier curve to substitute the direct summation of line segments. Figure 4 illustrates the optimization scheme of our proposed geodesic computational method. For each currently visited node P_0, instead of only searching its four-connectivity or eight-connectivity neighbors, we pick its 7×7 neighborhood and search all possible marching directions within this 7×7 window, as illustrated on the left-hand diagram. For each searching path (e.g. the path denoted by the purple arrow), we pick two more points, P_1 and P_2, in addition to the start point P_0 and end point P_3. After picking up the four points P_0–P_3, we then fit a cubic Bézier curve that can be formulated as follows:

$$B(t) = (1-t)^3 P_0 + 3(1-t)^2 t P_1 + 3(1-t)t^2 P_2 + t^3 P_3, \quad 0 \leqslant t \leqslant 1. \tag{7}$$

Then, the surface distance $d(P_0, P_3)$ between the nodes P_0 and P_3 is estimated as the arc length of the fitted Bézier curve.

$$d(P_0, P_3) = \int_0^1 |B'(t)|\,\mathrm{d}t, \tag{8}$$

where $B'(t)$ is the first-order derivative of the Bézier curve $B(t)$.

With this optimized scheme for geodesic computation, we can generate maps of geodesic distances $D_1(t,u,v)$ and $D_2(t,u,v)$ with respect to anchor points c_1 and c_2. Then, we extract a set of points $p_1(t)$ and $p_2(t)$ with equal geodesic distance d_1 and d_2, respectively, and perform a least-square fitting into spatial curves $\gamma_1[x(\tau), y(\tau), z(\tau)]$ and $\gamma_2[x(\tau), y(\tau), z(\tau)]$ of fourth-order polynomials. For instance, the parametric representation of a fourth-order spatial curve $\gamma[x(\tau), y(\tau), z(\tau)]$ can be expressed as

$$\begin{bmatrix} x & y & z \end{bmatrix}^T = M \begin{bmatrix} \tau^4 & \tau^3 & \tau^2 & \tau & 1, \end{bmatrix}^T \tag{9}$$

where M is a 3×5 coefficient matrix. The matching point $p(t)$ can be identified by the intersecting point of the spatial curves $\gamma_1[x(\tau), y(\tau), z(\tau)]$ and $\gamma_2[x(\tau), y(\tau), z(\tau)]$:

$$p(t) = \{(x, y, z) | \gamma_1(x, y, z) \cap \gamma_2(x, y, z)\}. \tag{10}$$

The numerical solution for this set of simultaneous nonlinear equations was computed using the MatLab *fsolve* function.

2.3. Strain computation

As is shown in figure 5, once we can determine the point-to-point correspondence between a current frame $S(t)$ and the initial frame $S(t_0)$, we can then calculate the Green–Lagrange strain tensor on that specific point. According to the Kirchoff–Love shell theory [29], the coefficients $E_{\alpha\beta}$ of the Green–Lagrange strain tensor can be modeled as [30, 31]

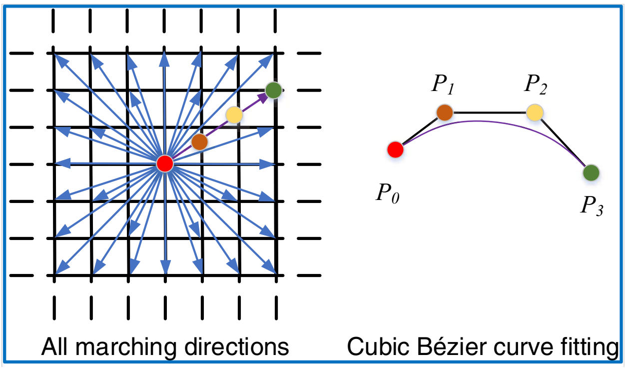

Figure 4. Optimization of Dijkstra's algorithm in accordance with our measured 3D data. Each grid point on the left figure denotes one 3D point corresponding to a camera pixel. For each currently visited point P_0, we pick its 7×7 neighborhood and search all possible marching directions as illustrated. For each searching path, we pick two more points in addition to the start and end point, and the distance is computed as the arc length of the interpolated cubic Bézier curve.

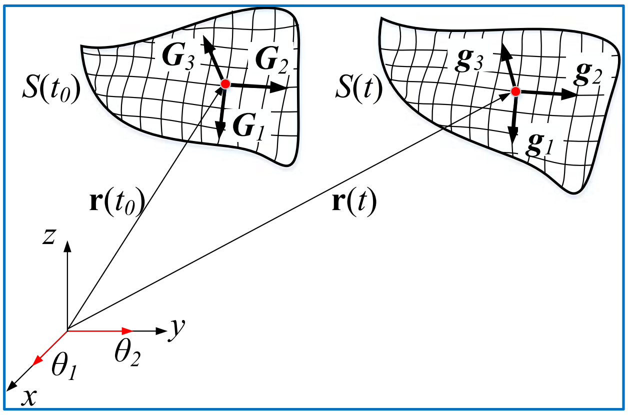

Figure 5. Notations in differential geometry. ($\mathbf{G}_\alpha$, $\mathbf{G}_\beta$) and ($\mathbf{g}_\alpha$, $\mathbf{g}_\beta$) are the base vectors of the tangent planes of the initial configuration $S(t_0)$ and the deformed surface $S(t)$; G_3 and g_3 are the corresponding normal vectors; $r(t_0)$ and $r(t)$ are the position vectors; θ_1 and θ_2 denote the surface parametrizations which coincide with world coordinate x and y in our research.

$$E_{\alpha\beta} = \varepsilon_{\alpha\beta} + \theta_3\kappa_{\alpha\beta}, \quad \alpha, \beta = 1, 2, \tag{11}$$

where $\alpha, \beta = 1, 2$ denotes the indexes of the matrix tensor; $\varepsilon_{\alpha\beta}$ denotes the membrane strain due to surface extension or compression; $\kappa_{\alpha\beta}$ represents the curvature changes due to bending, and θ_3 is the coordinate in thickness direction ($-0.5h \leqslant \theta_3 \leqslant 0.5h$, h represents the thickness).

Since the wings of our bird robot are made of a thin layer of inelastic plastic membrane with uniform thickness of h, according to Borg [32, 33], the elastic membrane strain $\varepsilon_{\alpha\beta}$ reduces to 0 and the model can be simplified as

$$E_{\alpha\beta} = -\frac{h}{2}\kappa_{\alpha\beta}. \quad \alpha, \beta = 1, 2. \tag{12}$$

The curvature change $\kappa_{\alpha\beta}$ is defined by the change in curvature tensor coefficients

$$\kappa_{\alpha\beta} = b_{\alpha\beta} - B_{\alpha\beta}, \quad \alpha, \beta = 1, 2, \tag{13}$$

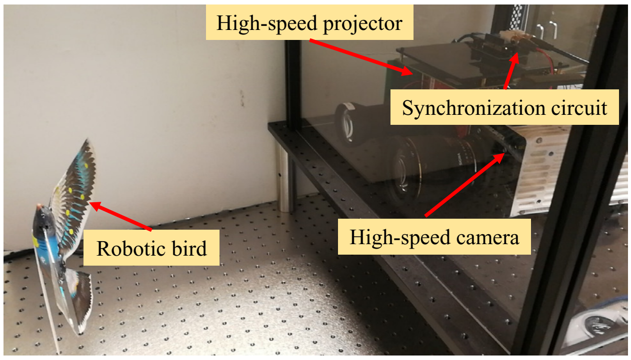

Figure 6. Photograph of the test system.

where $b_{\alpha\beta}$ and $B_{\alpha\beta}$ are, respectively, the curvature tensor coefficients of the point on the current and initial surface configuration. In fact, $b_{\alpha\beta}$ and $B_{\alpha\beta}$ are defined by the second fundamental forms of the surfaces. To compute their second fundamental forms, now suppose that we already found the corresponding points $p(t_0)$ and $p(t)$, respectively, on the initial undeformed and current deformed surfaces, we select a 15×15 pixels neighborhood for both $p(t_0)$ and $p(t)$ and fit them into quadratic surfaces $\mathbf{r}(\theta_1, \theta_2)$ as

$$x = \theta_1, \tag{14}$$

$$y = \theta_2, \tag{15}$$

$$z = A\theta_1^2 + B\theta_2^2 + C\theta_1\theta_2 + D\theta_1 + E\theta_2 + F. \tag{16}$$

We coincide θ_1 and θ_2 with the world coordinate x and y to ensure that our surfaces are using the same parameterization. Then, we find the tangent plane base vectors ($\mathbf{G}_1$, $\mathbf{G}_2$) and ($\mathbf{g}_1$, $\mathbf{g}_2$), respectively, from the initial undeformed state $S(t_0)$ and the current deformed state $S(t)$ as [30, 31]

$$(\mathbf{G}_1, \mathbf{G}_2) = \left[\frac{\partial \mathbf{r}(t_0)}{\partial \theta_1}, \frac{\partial \mathbf{r}(t_0)}{\partial \theta_2}\right], \tag{17}$$

$$(\mathbf{g}_1, \mathbf{g}_2) = \left[\frac{\partial \mathbf{r}(t)}{\partial \theta_1}, \frac{\partial \mathbf{r}(t)}{\partial \theta_2}\right]. \tag{18}$$

Then, the second-order partial derivatives can be computed as

$$\mathbf{G}_{\alpha\beta} = \frac{\partial^2 \mathbf{r}(t_0)}{\partial \theta_\alpha \partial \theta_\beta}, \quad \mathbf{g}_{\alpha\beta} = \frac{\partial^2 \mathbf{r}(t)}{\partial \theta_\alpha \partial \theta_\beta}. \quad \alpha, \beta = 1, 2. \tag{19}$$

Finally, the curvature tensor coefficients $b_{\alpha\beta}$ and $B_{\alpha\beta}$ can be computed by their corresponding second fundamental forms:

$$B_{\alpha\beta} = \mathbf{G}_{\alpha\beta} \cdot \mathbf{G_3}, \quad b_{\alpha\beta} = \mathbf{g}_{\alpha\beta} \cdot \mathbf{g_3}. \quad \alpha, \beta = 1, 2, \tag{20}$$

where $\mathbf{G}_3$ and $\mathbf{g}_3$ are, respectively, the normal vectors given by

$$\mathbf{G}_3 = \frac{\mathbf{G}_1 \times \mathbf{G}_2}{|\mathbf{G}_1 \times \mathbf{G}_2|}, \quad \mathbf{g}_3 = \frac{\mathbf{g}_1 \times \mathbf{g}_2}{|\mathbf{g}_1 \times \mathbf{g}_2|}. \tag{21}$$

Once we have computed the curvature tensor coefficients $b_{\alpha\beta}$ and $B_{\alpha\beta}$, we can compute the strain tensor coefficients $E_{\alpha\beta}$ by referring to equations (12) and (13). For visualization purposes, we demonstrate the strain maps in our later results (see figure 16) by extracting the dominant eigenvalue of the computed strain tensor.

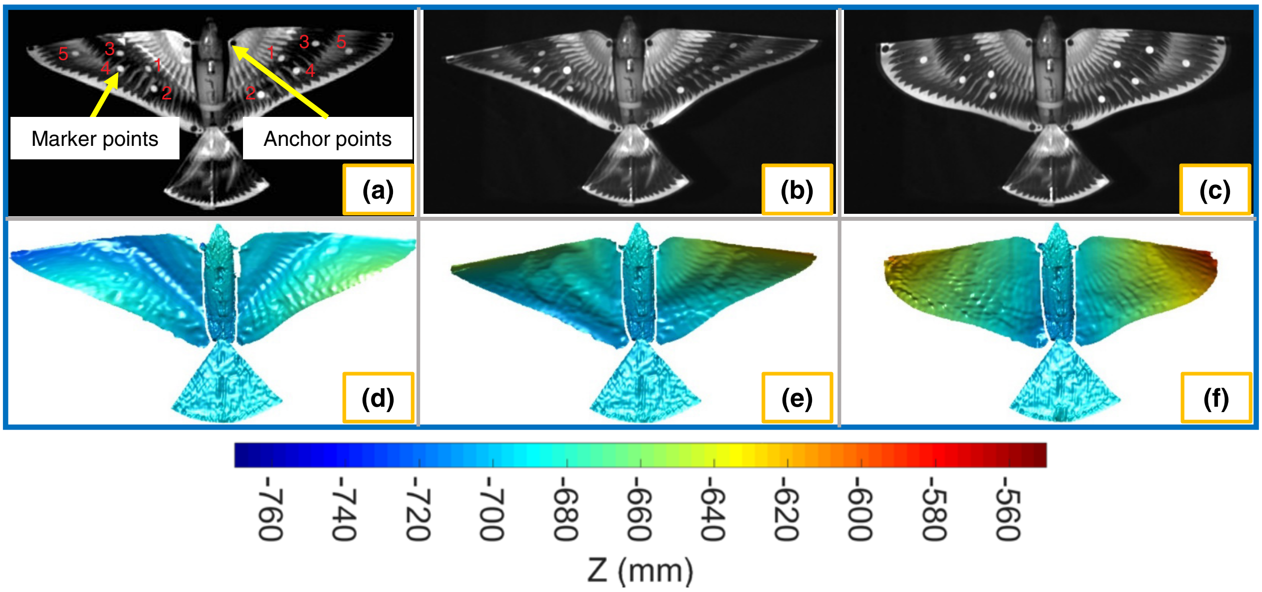

Figure 7. 3D measurement results of a flying bird robot with markers and anchor points for validation of our proposed point tracking. These markers are used to compare our point tracking scheme with the marker-based point tracking. (a)–(c) Three sample frames of 2D images from supplemental video S1; (d)–(f) three sample frames of 3D geometries from video S1.

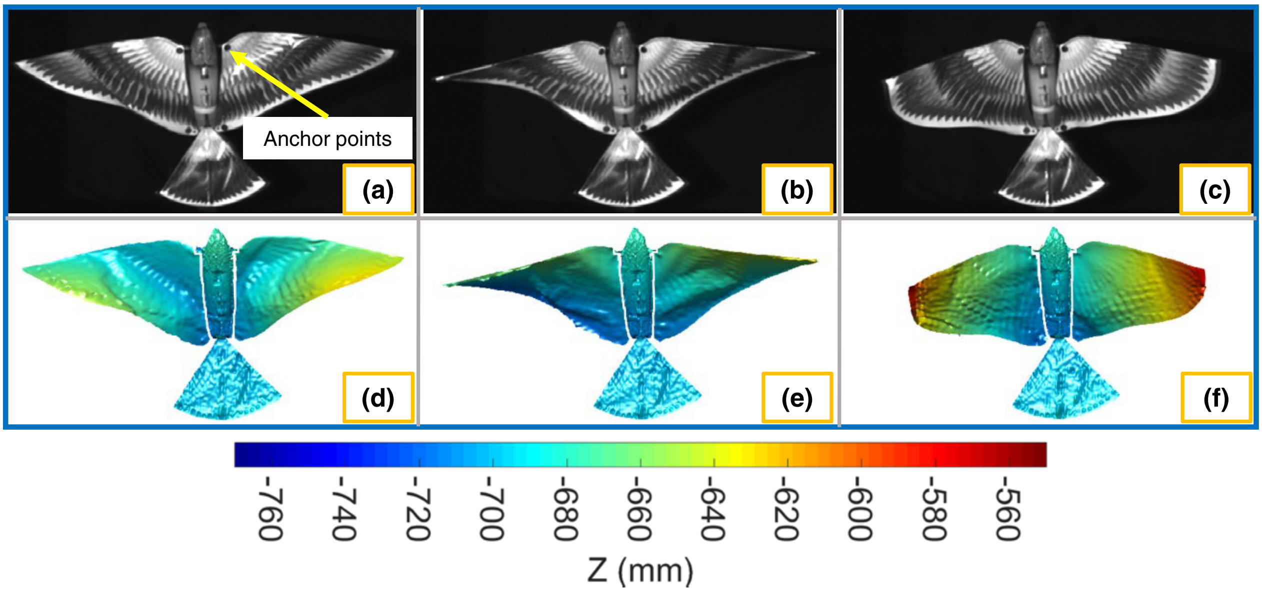

Figure 8. 3D measurement results of a flying bird robot with anchor points only for strain computation. The markers are removed to reduce potential mechanics changes. (a)–(c) Three sample frames of 2D images from supplemental video S2; (d)–(f) three sample frames of 3D geometries in supplemental video S2.

3. Results

3.1. Superfast 3D imaging of a robotic bird's flapping wing

We built a DFP system as shown in figure 6 for superfast 3D imaging. The system is composed of a high-speed DLP projector (Wintech PRO 6500) for fringe projection and a high-speed CMOS camera (NAC MEMRECAM GX-8F) for image acquisition. The fringe projection speed was set as 5000 Hz with an image resolution of 1920×1080 pixels. Precisely synchronized with the fringe projection, the camera captures images also at a rate of 5000 Hz with an image resolution of 800×600 pixels. A lens (SIGMA 24 mm f/1.8 EX DG) with a focal length of 24 mm is attached to the camera whose aperture ranges from f/1.8 to f/22. The robotic bird (XTIM Bionic Bird Avitron version 2.0) that we used in this research has a beat frequency of approximately 25 cycles per second with both wings made of inextensible thin membranes. The rib is made of a single metal bar positioned on the upper boundary of the wing. The total span of a single wing is about 150 mm (L) $\times$ 70 mm (W). We employed a modified FTP method [18] for 3D reconstruction. In our strain evaluation, we performed analysis with 30 803 and 29 840 points on the left and right wing, respectively, which equals the total number of pixels that the wings occupy in our initial frame. We took the first 100 frames for 3D reconstruction and strain analysis.

Table 1. Validation of our geometry-based point tracking by comparing with the marker based tracking. Diff = difference.

Marker #	Diff X (Mean)	Diff Y (Mean)	Diff Z (Mean)	Diff X (RMS)	Diff Y (RMS)	DiffZ(RMS)
Lett wing						
1	0.05 mm	0.42 mm	0.15 mm	0.39 mm	0.75 mm	0.37 mm
2	0.56 mm	0.73 mm	0.02 mm	0.72 mm	0.78 mm	0.21 mm
3	0.06 mm	0.40 mm	0.13 mm	0.80 mm	1.06 mm	0.48 mm
4	0.17 mm	0.18 mm	0.02 mm	0.42 mm	0.67 mm	0.29 mm
5	0.08 mm	1.17 mm	0.51 mm	0.53 mm	1.24 mm	1.05 mm
Right wing						
1	0.02 mm	0.42 mm	0.20 mm	0.35 mm	0.19 mm	0.17 mm
2	0.13 mm	0.45 mm	0.17 mm	0.77 mm	0.28 mm	0.26 mm
3	0.27 mm	0.30 mm	0.35 mm	1.19 mm	0.37 mm	0.36 mm
4	0.45 mm	0.72 mm	0.22 mm	0.84 mm	0.40 mm	0.20 mm
5	0.61 mm	0.94 mm	0.76 mm	1.14 mm	0.48 mm	0.86 mm

We captured two sets of 3D data in preparation for further strain analysis: (1) with both two anchor points (black) on the corner and five marker points (white) inside of each robot wing (see figures 7(a)–(c)); (2) with only two anchor points (black) on the corner of each robot wing (see figures 8(a)–(c)). We used our first dataset to validate our proposed point-tracking method by comparing it with conventional marker-based point tracking; then, we used our second dataset to perform strain computation. Since our proposed method does not need those markers inside of the wings, we removed them in our second dataset to reduce the potential mechanics changes caused by markers. The purpose of anchor points is to assist our proposed geometry-based point tracking. Figures 7(d)–(f) (supplemental video S1 (stacks.iop.org/MST/29/045402/mmedia)) and figures 8(d)–(f) (supplemental video S2), respectively, show the reconstructed 3D geometries of both datasets. From which we can see that our proposed 3D measurement algorithm consistently works well for the entire dynamic flapping flight processes of the bird robot.

3.2. Validation of point tracking

Once the dynamic 3D data is obtained, the next task is to perform point tracking so that the strain can be computed by examining the surface deformation. Here we propose a novel point tracking method based on geodesic computation. Given that we are investigating inextensible surfaces, the theoretical foundation of our proposed point tracking method is that topological changes will not change the shortest distances of any two points on the surface. Therefore, for any point inside of the wings in one 3D frame, we locate its corresponding point in other 3D frames by computing its geodesic distances to the two anchor points. This conceptual idea is shown in figure 2 and the detailed principles are discussed in the Methods section.

We used our first dataset shown in figure 7 to compare our proposed point tracking with conventional marker-based tracking. We performed the comparison by examining the differences of the extracted trajectories in X, Y and Z from both methods. Table 1 shows both the mean and the root-mean-square (RMS) differences. The maximum mean difference is about 1.2 mm for X and Y, and 0.80 mm for Z; the maximum RMS difference is about 1.2 mm for X and Y, and 1.0 mm for Z. Considering the total span of a single wing (i.e. 150 mm (L) × 70 mm (W)), this difference is relatively small. For visualization, here we show two different comparison results of the left wing in figures 9 and 10, which corresponds to the ones with least (marker 4) and most (marker 5) differences. We overlaid the extracted X, Y and Z trajectories from our proposed method (blue solid line) with the ones directly extracted from circle centers (red dashed line), from which we can see the overall extracted trajectories from the two methods are pretty similar. The results show that our proposed geometry-based method can achieve very similar point tracking compared to the conventional marker based method, which demonstrates the success of our proposed point tracking framework.

To evaluate the smoothness of our point tracking method, we take the marker with larger tracking difference (marker 5) as an example, and then compute its velocity and acceleration for the data obtained both from direct marker tracking and our proposed method. Figures 11 and 12, respectively, show the velocity and acceleration curves from the data in figure 10. Overall, the mean and RMS differences for velocity are between 0.01–0.02 mm ms^{-1} and 0.1–0.2 mm ms^{-1}, respectively; the mean and RMS differences for acceleration are between 0.001–0.004 mm ms^{-2} and 0.04–0.06 mm ms^{-2}, respectively. This result clearly demonstrates that our point tracking is as smooth as direct marker tracking, which can potentially benefit the wing dynamics analysis.

To further validate our proposed method, we compared our point tracking approach with the well-known digital image correlation (DIC) [34–37] technology. Essentially, DIC is a well-established technology for mechanics testing in the optics field. The DIC computes the displacement field by identifying similar points in different images through textural analysis. Therefore, such technology requires the sampled surface to present a strongly varying texture or to perform random speckle painting.

We first used our second dataset (without markers) shown in figure 8 to extract the displacement field using both DIC and our method. The open source DIC software *Ncorr* [38] is used to perform image correlation analysis. Figure 13 shows a sample frame of computed horizontal and vertical displacement fields. The result clearly shows that our method can

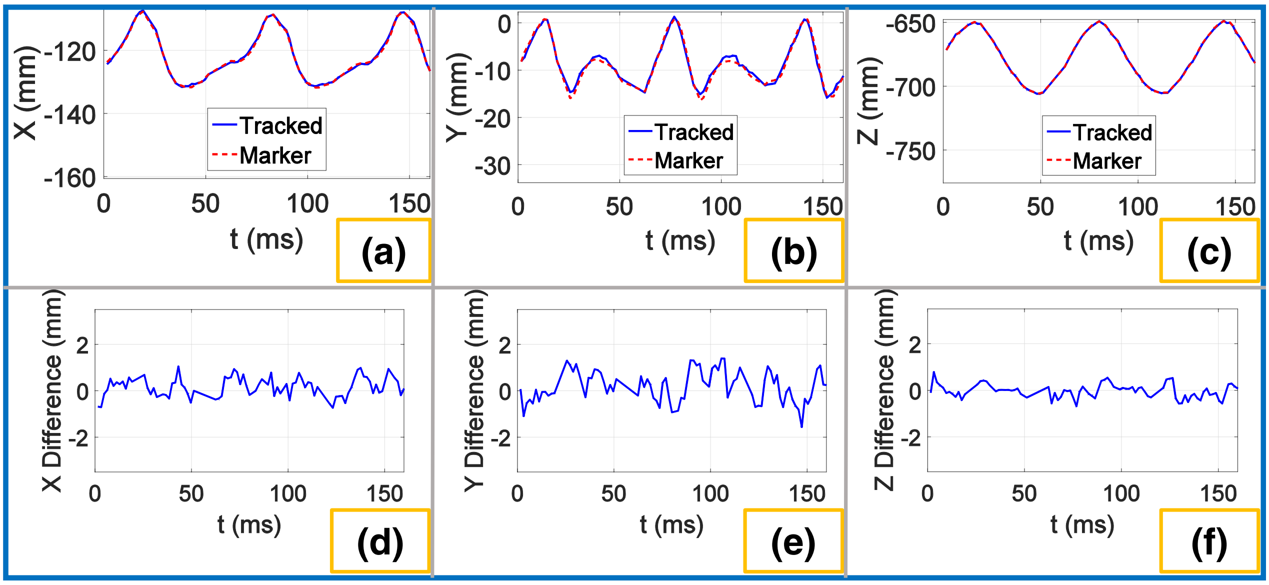

Figure 9. Visualization of tracking for marker point 4 of the left wing. (a)–(c) Overlay of the directly extracted marker points (red dashed lines) with tracked marker points (blue solid lines) using geodesic computation under X, Y and Z coordinates; (d)–(f) the difference plots of (a)–(c) obtained by taking the difference of curves, the mean differences for X, Y and Z are 0.17 mm, 0.18 mm and 0.02 mm, respectively; the RMS difference for X, Y and Z are 0.42 mm, 0.67 mm and 0.29 mm, respectively.

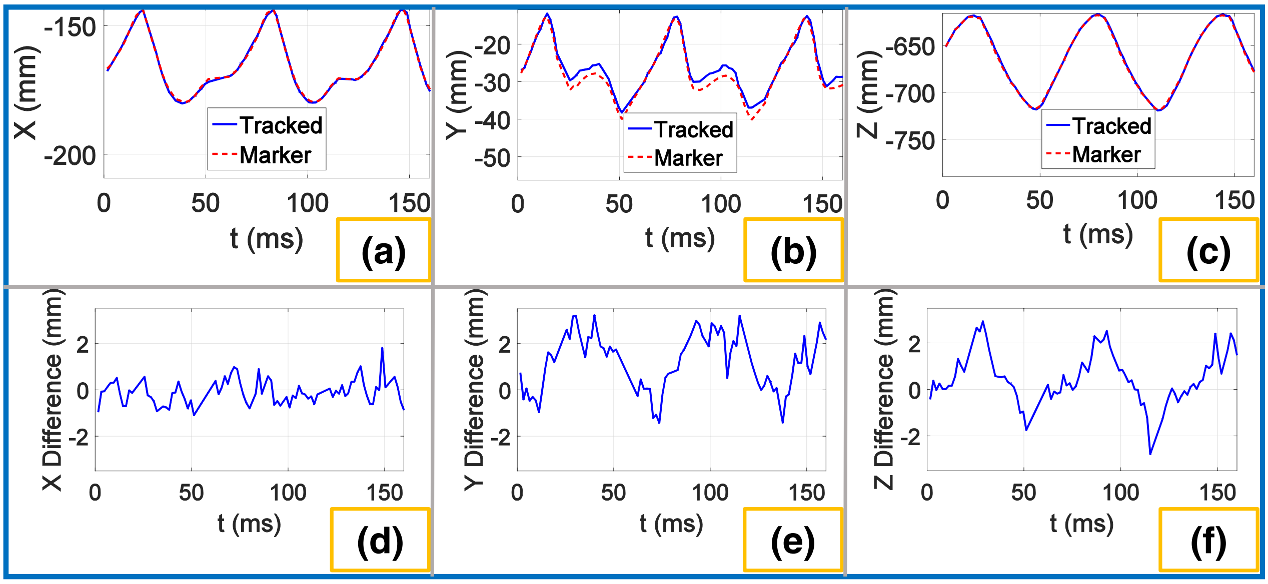

Figure 10. Visualization of tracking for marker point 5 of the left wing. (a)–(c) Overlay the directly extracted marker points (red dashed lines) with tracked marker points (blue solid lines) using geodesic computation under X, Y and Z coordinates; (d)–(f) the difference plots of (a)–(c) are obtained by taking the difference of curves. The mean differences for X, Y and Z are 0.08 mm, 1.17 mm and 0.51 mm, respectively; the RMS difference sfor X, Y and Z are 0.53 mm, 1.24 mm and 1.05 mm, respectively.

extract the full displacement field yet the DIC method fails in some specific regions. This is due to the fact that the wings shown in the images present weak or repetitive features in particular regions, which is challenging for image correlation analysis. Also, large bending will further weaken the point similarities between images. In contrast, our method is based on surface geometric analysis, which does not require analyzing textural variations. Thus, it is less likely to fail given the aforementioned conditions.

For accuracy validation, we selected one obvious feature on each wing (highlighted as cross markers on the top left image of figure 13), and then compared the point tracking between DIC and our method. Figures 14 and 15 show the tracked motion trajectories and the corresponding errors plots. The results show that, for these feature points, our method can provide a tracking accuracy comparable to DIC. Moreover, DIC fails in quite a few number of frames, while our method still prevails. Overall, for both DIC and our proposed method, the mean and RMS errors are around 0.1–0.3 mm and 0.3–0.6 mm, respectively. For fair comparison, the mean and RMS errors we provided are based on data points where both methods survive. The result demonstrates that our proposed method can achieve an accuracy similar to the well-established DIC method, while our method can achieve a higher

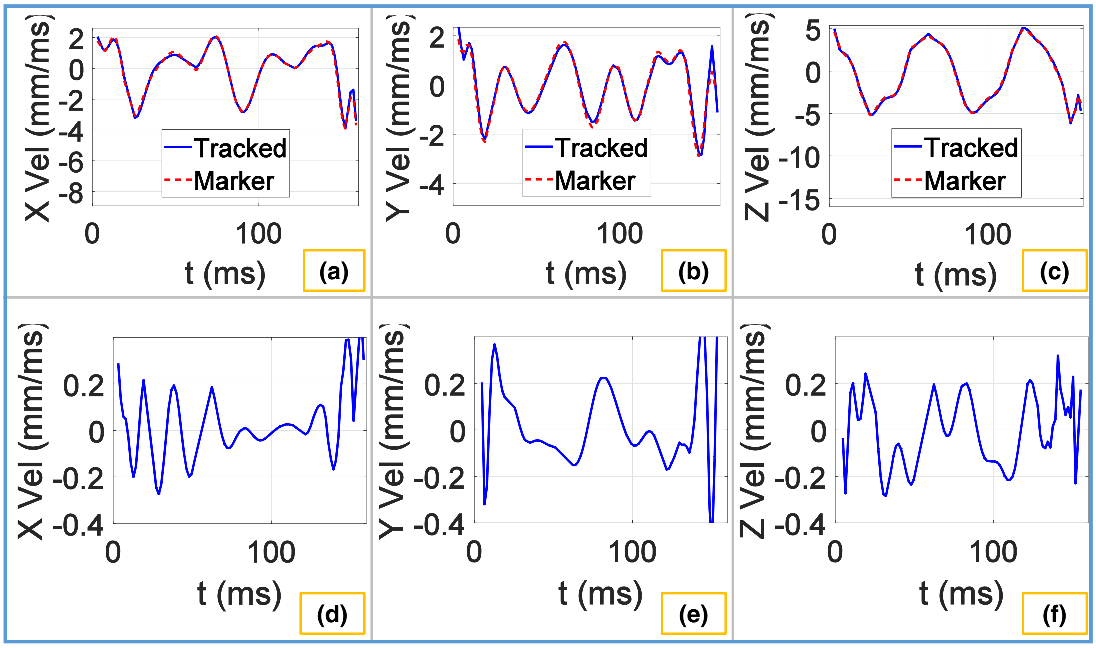

Figure 11. Visualization of velocity for marker point 5 of the left wing. (a)–(c) Overlay of the directly extracted marker velocity (red dashed lines) with tracked marker velocity (blue solid lines) using geodesic computation under *X*, *Y* and *Z* coordinates; (d)–(f) the difference plots of (a)–(c) obtained by taking the difference of curves; the mean differences for *X*, *Y* and *Z* are 0.01 mm ms^{-1}, 0.02 mm ms^{-1} and 0.01 mm ms^{-1}, respectively; the RMS differences for *X*, *Y* and *Z* are 0.13 mm ms^{-1}, 0.20 mm ms^{-1} and 0.15 mm ms^{-1}, respectively.

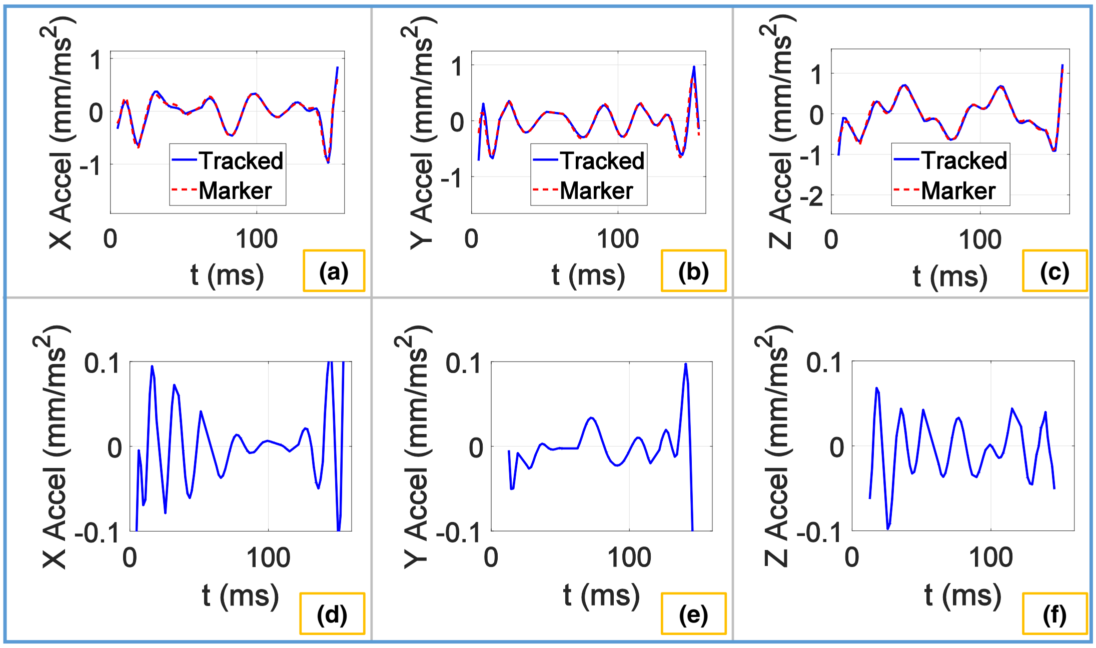

Figure 12. Visualization of acceleration for marker point 5 of the left wing. (a)–(c) Overlay of the directly extracted marker acceleration (red dashed lines) with tracked marker acceleration (blue solid lines) using geodesic computation under *X*, *Y* and *Z* coordinates; (d)–(f) the difference plots of (a)–(c) obtained by taking the difference of curves, the mean differences for *X*, *Y* and *Z* are 0.001 mm ms^{-2}, 0.001 mm ms^{-2} and 0.004 mm ms^{-2}, respectively; the RMS differences for *X*, *Y* and *Z* are 0.04 mm ms^{-2}, 0.06 mm ms^{-2} and 0.04 mm ms^{-2}, respectively.

success rate than DIC over the entire sampled image if a special surface treatment is unavailable.

3.3. Visualization of the strain map

Since we have validated that our proposed point tracking method can work well, we can now perform strain computation using the second dataset shown in figure 8. As mentioned above, to reduce potential mechanics changes, we removed the markers inside of the wings in our second dataset given that our point tracking method does not need them. Since the wings are inextensible, here we mainly consider the bending strain in a Green–Lagrange strain tensor. For each point on the wings that is tracked between different frames, the bending

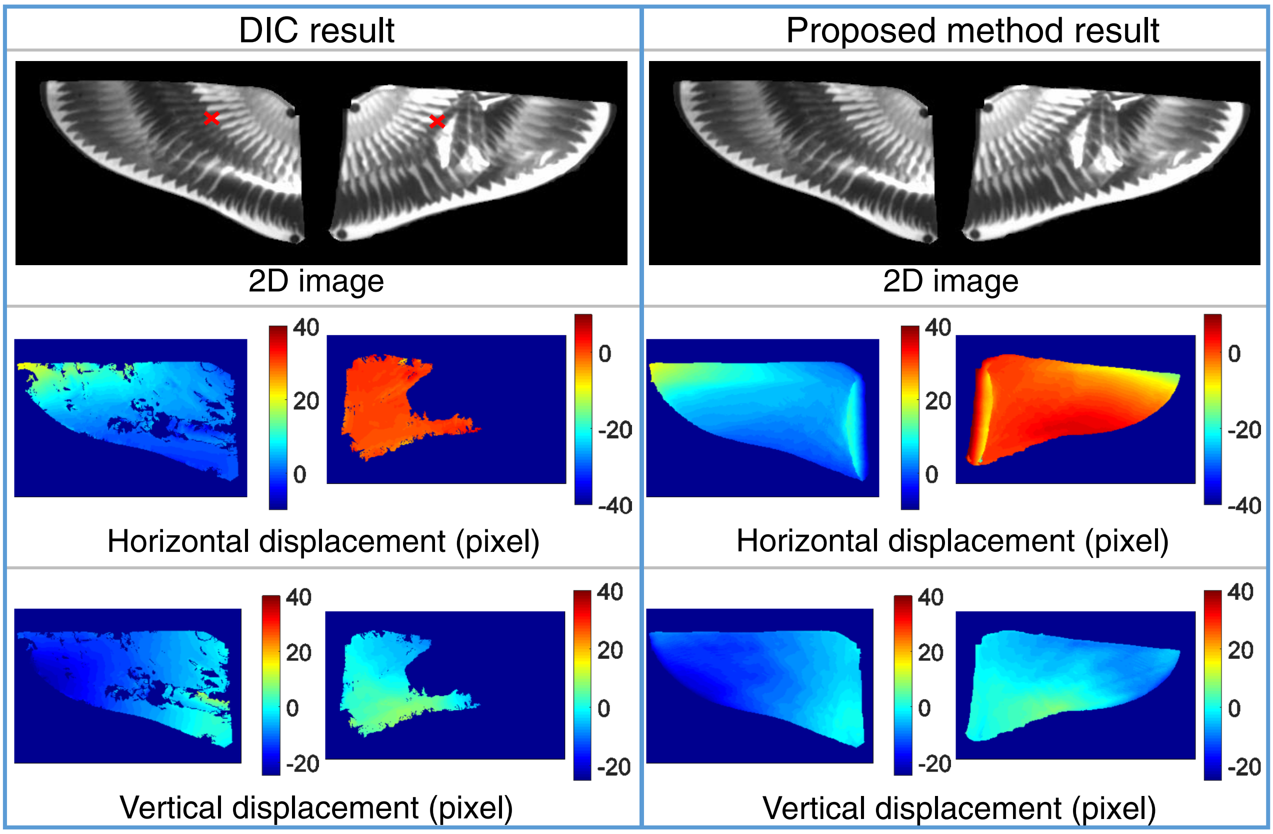

Figure 13. Results of extracted displacement field from both DIC and the proposed method.

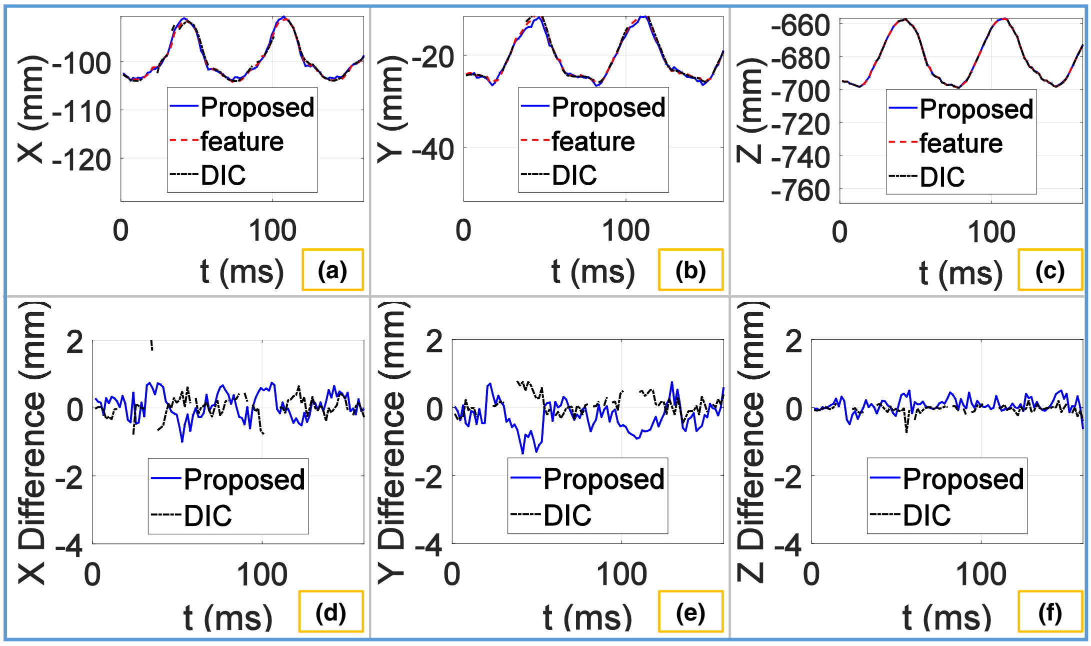

Figure 14. Validation of point tracking of the left wing feature point. (a)–(c) Overlay of the extracted feature X, Y and Z trajectories with the tracked point trajectories using DIC and the proposed method; (d)–(f) corresponding errors plots of both DIC and the proposed method. The X, Y and Z mean errors are 0.07 mm, 0.10 mm and −0.05 mm for DIC, and 0.08 mm, −0.28 mm and 0.07 mm for the proposed method; the X, Y and Z RMS errors are 0.43 mm, 0.28 mm and 0.13 mm for DIC, and 0.37 mm, 0.41 mm and 0.20 mm for proposed method.

strain can be computed by examining the curvature changes. The theoretical background of strain computation is discussed in the Methods section.

Figure 16 (supplemental video S3) shows the results of our strain computation. It illustrates that our method can compute the strains of the entire wings. Here we show a sample frame of an up-stroke and a down-stroke, respectively. One can notice that the wings are mostly strained on areas where we see the most bending or curvature, which agrees well with the nature of bending strain. This result demonstrates the success

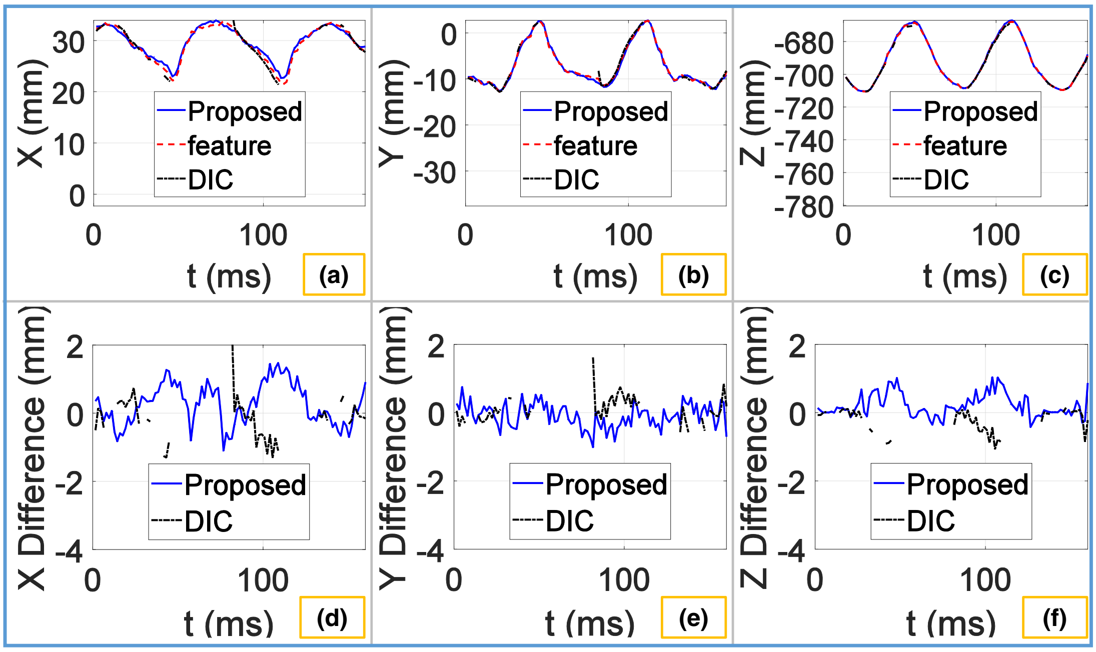

Figure 15. Validation of point tracking of the right wing feature point. (a)–(c) Overlay of the extracted feature X, Y and Z trajectories with the tracked point trajectories using DIC and proposed method; (d)–(f) corresponding errors plots of both DIC and the proposed method. The X, Y and Z means errors are -0.16 mm, 0.11 mm and -0.25 mm for DIC, and 0.26 mm, -0.08 mm and 0.21 mm for the proposed method; the X, Y and Z RMS errors are 0.67 mm, 0.39 mm and 0.34 mm for DIC, and 0.60 mm, 0.34 mm and 0.33 mm for the proposed method.

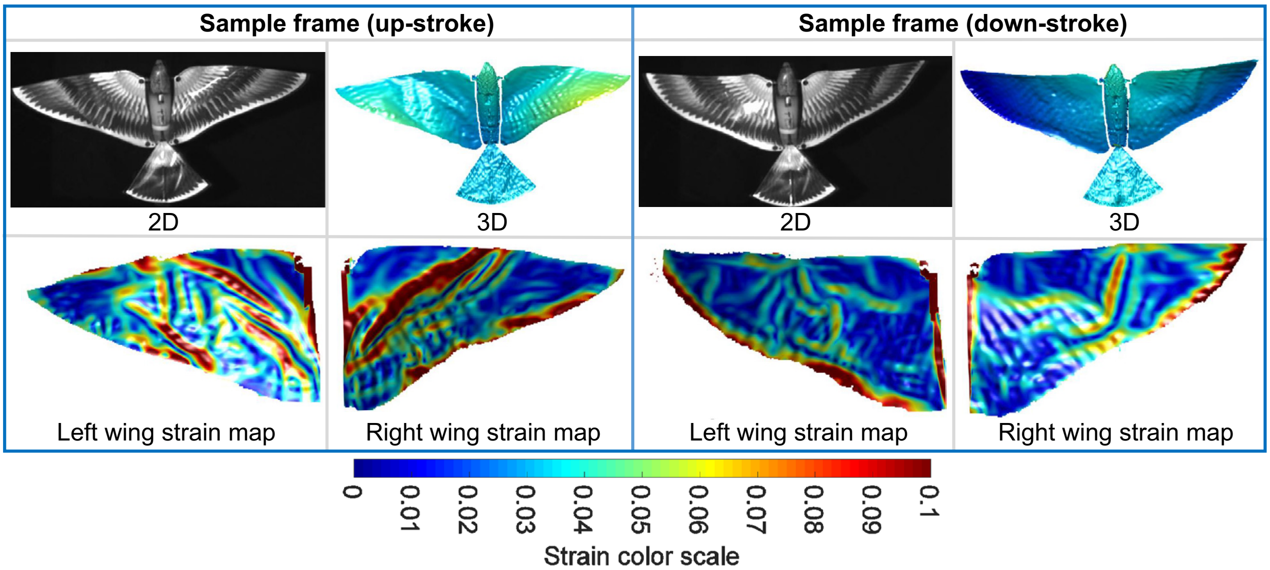

Figure 16. Two sample frames of the strain measurement result in supplemental video S3.

of our proposed strain computational framework. The computed strain maps can be easily turned into stress maps if we know the modulus of the wing material in advance.

4. Discussion

Compared to existing technologies, our proposed research has the following advantages:

- *Measures both high-resolution 3D geometry and the full-field wing strain map.* Our measurement technology can measure 3D geometry with high spatial and temporal resolution, and compute full-field strain for the wings. By providing this information, our technology could be effective tools for the robotics field for the study of wing morphology and mechanics analysis.
- *Requires only two anchor points on the corners.* Our point tracking scheme only requires identifying two anchor points on the corners. It neither requires putting markers inside of the wings nor a special surface treatment on the wing surfaces, which reduces the potential changes of flight mechanics during measurements.

Despite the aforementioned merits, our strain measurements could encounter challenges when the wings contain membrane or tension strain. In our strain analysis, we performed point tracking based on the assumption that the wing is an inextensible surface. For isometric wings, our algorithm can be adaptable if the ratio of surface expansion can be determined beforehand. However, it could be challenging to adapt our technology to measurements of non-isometric wings. Future work is possible to develop more sophisticated algorithms for non-isometric analysis if some *a priori* knowledge of the dynamics or a physical model of the wings can be obtained.

5. Conclusion

In this research, we introduced a novel method for dynamic dense strain measurement of robotic flapping wings. We first established a 5000 Hz DFP system with defocused binary pattern projection for superfast 3D imaging. Then, we developed a novel dense strain computational framework for the acquired dynamic 3D data. Our developed strain computational framework has two major components: (1) a novel geodesic-based point tracking scheme without using many fiducial markers; and (2) a strain computation scheme based on the Kirchhoff–Love shell theory. Experiments have demonstrated the success of both superfast 3D imaging and strain measurement with validations in point tracking.

Acknowledgments

The authors would like to thank laboratory members of the XYZT lab of Purdue University for their advice and support. We would like to give our special thanks to Professor Adrian Buganza Tepole at Purdue University for his valuable advice. This work was conducted when Beiwen Li was at Purdue University [39]. This research was sponsored by National Science Foundation under grant number CMMI-1531048.

ORCID iDs

Beiwen Li https://orcid.org/0000-0001-8130-7730

References

[1] Hedrick T L, Combes S A and Miller L A 2014 Recent developments in the study of insect flight *Can. J. Zool.* **93** 925–43

[2] Song D, Wang H, Zeng L and Yin C 2001 Measuring the camber deformation of a dragonfly wing using projected comb fringe *Rev. Sci. Instrum.* **72** 2450–4

[3] Nachtigall W 2000 Insect wing bending and folding during flight without and with an additional prey load *Entomol. Generalis* **25** 1–16

[4] Zeng L, Matsumoto H and Kawachi K 1996 A fringe shadow method for measuring flapping angle and torsional angle of a dragonfly wing *Meas. Sci. Technol.* **7** 776

[5] Zeng L, Hao Q and Kawachi K 2000 A scanning projected line method for measuring a beating bumblebee wing *Opt. Commun.* **183** 37–43

[6] Wang H, Zeng L, Liu H and Yin C 2003 Measuring wing kinematics, flight trajectory and body attitude during forward flight and turning maneuvers in dragonflies *J. Exp. Biol.* **206** 745–57

[7] Sunada S, Song D, Meng X, Wang H, Zeng L and Kawachi K 2002 Optical measurement of the deformation, motion, and generated force of the wings of a moth, *Mythimna separata* (walker) *JSME Int. J. Ser.* B **45** 836–42

[8] Koehler C, Liang Z, Gaston Z, Wan H and Dong H 2012 3d reconstruction and analysis of wing deformation in free-flying dragonflies *J. Exp. Biol.* **215** 3018–27

[9] Walker S M, Thomas A L and Taylor G K 2009 Photogrammetric reconstruction of high-resolution surface topographies and deformable wing kinematics of tethered locusts and free-flying hoverflies *J. R. Soc. Interface* **6** 351–66

[10] Ren Y, Dong H, Deng X and Tobalske B 2016 Turning on a dime: asymmetric vortex formation in hummingbird maneuvering flight *Phys. Rev. Fluids* **1** 050511

[11] Tobalske B W, Warrick D R, Clark C J, Powers D R, Hedrick T L, Hyder G A and Biewener A A 2007 Three-dimensional kinematics of hummingbird flight *J. Exp. Biol.* **210** 2368–82

[12] Willmott A P and Ellington C P 1997 The mechanics of flight in the hawkmoth *Manduca sexta*. I. Kinematics of hovering and forward flight *J. Exp. Biol.* **200** 2705–22

[13] Wootton R J 1993 Leading edge section and asymmetric twisting in the wings of flying butterflies (insecta, papilionoidea) *J. Exp. Biol.* **180** 105–17

[14] Norberg U M L and Winter Y 2006 Wing beat kinematics of a nectar-feeding bat, *Glossophaga soricina*, flying at different flight speeds and Strouhal numbers *J. Exp. Biol.* **209** 3887–97

[15] Albertani R, Stanford B, Hubner J and Ifju P 2007 Aerodynamic coefficients and deformation measurements on flexible micro air vehicle wings *Exp. Mech.* **47** 625–35

[16] Zhang S 2010 Recent progresses on real-time 3D shape measurement using digital fringe projection techniques *Opt. Laser Eng.* **48** 149–58

[17] Dijkstra E W 1959 A note on two problems in connexion with graphs *Numer. Math.* **1** 269–71

[18] Guo L, Su X and Li J 1990 Improved Fourier transform profilometry for the automatic measurement of 3D object shapes *Opt. Eng.* **29** 1439–44

[19] Li B, Liu Z and Zhang S 2016 Motion induced error reduction by combining Fourier transform profilometry with phase-shifting profilometry *Opt. Express* **24** 23289–303

[20] Lei S and Zhang S 2009 Flexible 3D shape measurement using projector defocusing *Opt. Lett.* **34** 3080–2

[21] Ajubi G A, Ayubi J A, Martino J M D and Ferrari J A 2010 Pulse-width modulation in defocused 3D fringe projection *Opt. Lett.* **35** 3682–4

[22] Lohry W and Zhang S 2012 Fourier transform profilometry using a binary area modulation technique *Opt. Eng.* **51** 113602

[23] Wang Y and Zhang S 2012 Three-dimensional shape measurement with binary dithered patterns *Appl. Opt.* **51** 6631–6

[24] Zhang S, van der Weide D and Oliver J 2010 Superfast phase-shifting method for 3D shape measurement *Opt. Express* **18** 9684–9

[25] Lohry W and Zhang S 2012 3d shape measurement with 2D area modulated binary patterns *Opt. Laser Eng.* **50** 917–21

[26] Jellett J H 1849 On the properties of inextensible surfaces *Trans. R. Ir. Acad.* **22** 343–77

[27] Sethian J A 1996 A fast marching level set method for monotonically advancing fronts *Proc. Natl Acad. Sci.* **93** 1591–5
[28] Sethian J A 1999 *Level Set Methods and Fast Marching Methods: Evolving Interfaces in Computational Geometry, Fluid Mechanics, Computer Vision, and Materials Science* vol 3 (Cambridge: Cambridge University Press)
[29] Love A E H 1888 The small free vibrations and deformation of a thin elastic shell *Phil. Trans. R. Soc. Lond.* A **179** 491–546
[30] Kiendl J, Bletzinger K-U, Linhard J and Wüchner R 2009 Isogeometric shell analysis with Kirchhoff–Love elements *Comput. Methods Appl. Mech. Eng.* **198** 3902–14
[31] Kiendl J, Hsu M-C, Wu M C and Reali A 2015 Isogeometric Kirchhoff–Love shell formulations for general hyperelastic materials *Comput. Methods Appl. Mech. Eng.* **291** 280–303
[32] Borg S F 1962 A specialized nonlinear thin plate inextensional bending theory *J. Franklin Inst.* **274** 98–114
[33] Borg S F 1990 *Matrix-Tensor Methods in Continuum Mechanics* (Singapore: World Scientific)
[34] Peters W and Ranson W 1982 Digital imaging techniques in experimental stress analysis *Opt. Eng.* **21** 213427
[35] Chu T, Ranson W and Sutton M 1985 Applications of digital-image-correlation techniques to experimental mechanics *Exp. Mech.* **25** 232–44
[36] Sutton M, Mingqi C, Peters W, Chao Y and McNeill S 1986 Application of an optimized digital correlation method to planar deformation analysis *Image Vis. Comput.* **4** 143–50
[37] Pan B, Qian K, Xie H and Asundi A 2009 Two-dimensional digital image correlation for in-plane displacement and strain measurement: a review *Meas. Sci. Technol.* **20** 062001
[38] Blaber J, Adair B and Antoniou A 2015 Ncorr: open-source 2D digital image correlation MATLAB software *Exp. Mech.* **55** 1105–22
[39] Li B 2017 Superfast 3D shape measurement with application to flapping wing mechanics analysis *PhD Thesis* Purdue University